



Reliable phase quantification in focused probe electron ptychography of thin materials

Christoph Hofer, Timothy J. Pennycook*

EMAT, University of Antwerp, Groenenborgerlaan 171, 2020 Antwerp, Belgium

ARTICLE INFO

Keywords:

Single side band ptychography
Phase retrieval
Quantification

ABSTRACT

Electron ptychography provides highly sensitive, dose efficient phase images which can be corrected for aberrations after the data has been acquired. This is crucial when very precise quantification is required, such as with sensitivity to charge transfer due to bonding. Drift can now be essentially eliminated as a major impediment to focused probe ptychography, which benefits from the availability of easily interpretable simultaneous Z-contrast imaging. However challenges have remained when quantifying the ptychographic phases of atomic sites. The phase response of a single atom has a negative halo which can cause atoms to reduce in phase when brought closer together. When unaccounted for, as in integrating methods of quantification, this effect can completely obscure the effects of charge transfer. Here we provide a new method of quantification that overcomes this challenge, at least for 2D materials, and is robust to experimental parameters such as noise, sample tilt.

1. Introduction

Electron ptychography addresses the phase retrieval problem in transmission electron microscopy [1], using the probe position dependence of the convergent beam electron diffraction. Ptychography takes advantage of redundancy in the diffraction data, either via overlapping probe positions or overlapping diffracted beams. Before the success of aberration correction in hardware, direct focused probe ptychography was successfully applied to resolve the atomic structure at a resolution three times the conventional limit a scanning transmission electron microscope (STEM) with its ability to achieve superresolution [2]. With the rise of aberration correction in hardware, atomic resolution became largely routine for many materials, and the limits of electron microscopy shifted more to the robustness of the sample to the electron beam in many cases. However ptychography is useful for much more than superresolution, and a primary feature of the technique is its very high dose efficiency, which can even exceed the dose-efficiency of aberration-corrected high-resolution transmission electron microscopy (HRTEM) [3]. This efficiency is of great interest for beam sensitive samples, but also when the need for extreme sensitivity and precision arises, as is the case for accurate measurements of charge density, especially when one wishes to detect the subtle effect of charge transfer due to bonding.

To overcome the scan speed limitations imposed by slow cameras, electron ptychography can be performed using a defocused probe setup, which allows one to utilize far fewer probe positions for a given

area [4,5]. This can be useful for low dose applications, as the electrons are then distributed over a larger area [6]. Now cameras have exceeded MHz readout times allowing one to capture truly fast 4D data sets with a focused, atomically sharp probe [7]. This allows one to avoid both the high doses and distortions due to drift associated with slow scans and simultaneously capture the higher angle scattering for annular dark field (ADF) Z-contrast imaging, which would be out of focus with a defocused probe. This is an extremely useful configuration as the phase images provide the greatest sensitivity to all the atoms, and indeed electrons, while the Z-contrast ADF image remains very useful for its ease of interpretation and ability to distinguish heavier elements [8,9].

Phase images are sensitive to the total potential in the material, including the contribution from electrons in addition to the nuclear potential, enabling charge density mapping [10–12] and even detection of charge transfer [13,14]. However, detecting charge transfer is particularly challenging and requires a robust and reliable method to quantify the phases of atomic sites. Numerous publications successfully address the quantification of atomic intensities with the ADF signal [15–17]. Phase contrast images are, however, significantly more complicated to analyze as the contrast transfer function is generally more complex [18, 19].

Single side band (SSB) ptychography is a fast, direct phase retrieval method in STEM, extracting the phase by integrating over the double disk overlaps in probe reciprocal space [20]. Problems quantifying SSB,

* Corresponding author.

E-mail address: timothy.pennycook@uantwerpen.be (T.J. Pennycook).

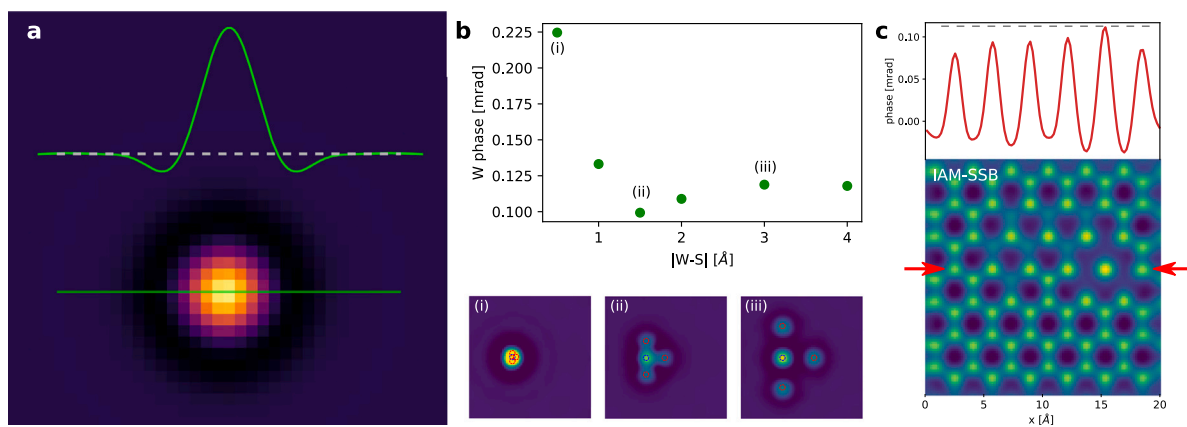


Fig. 1. Example of the negative halo appearing around atomic sites in SSB ptychographic images and the resulting dependence of atomic phases on the distance to neighboring atoms. (a) SSB image of isolated W with a line profile taken across the center of the atom showing the negative halo. The dashed lines in the plot of the line profile indicate 0 phase. (b) Examining the SSB phase variation of neighboring single atoms as a function of their distance. The plot shows the phase at the center of a W atom vs the distance to three neighboring S atoms. The S atoms are moved outwards from the W atom as indicated in the SSB images at the bottom, using a green circle to indicate the W site and red circles to label the S atoms. Because of the negative halo, the phase at the center of W atom displays a minimum when the negative halos from the atomic sites coincide. (c) This is important to take into account when analyzing SSB images such as this simulation of defective WS_2 , which shows a significant variation of the W profile depending on positions of the neighboring atoms.

or other ptychographic images, are revealed when analyzing phase images of single atoms, such as those shown in Fig. 1. Unlike ADF images, an SSB phase image displays a negative halo around a single atom, before converging to a zero valued background. This negative contribution makes quantification difficult, as the negative tail can influence the phase of neighboring atoms. Fig. 1b shows the phase at the center of a single W atom as a function of the distance to three neighboring S atoms. At small distances, the atomic phases significantly overlap and add up to a large integrated phase. This occurs with any imaging technique as the distance of the atoms are smaller than the resolution limit of the microscopic setup. Increasing the distance decreases the W phase and separates the atoms. Importantly, however, the phase reaches a minimum and increases again before reaching a plateau corresponding to the phase of an isolated independent atom. The occurrence of a local minimum is a result of the negative halo of the atomic phase.

The negative halo can cause the phase of the same type of atom to vary significantly depending on the configuration of the atoms surrounding it, which can hamper quantification. To demonstrate this, we simulated an SSB image of a defective area of monolayer WS_2 , introducing several S vacancies to change the local environment of certain W atoms. This is shown in Fig. 1c. We also included a quasi isolated W atom surrounded by 3 S divacancies, which is not physically stable but is a useful demonstration of the difficulty of phase quantification. A line profile across the W atoms shows a clear variation of the observed phases. The highest phase is the quasi-isolated W site while the lowest W phase is the pristine site without vacancies. This is because the quasi-isolated W atom is not influenced by the negative contribution of neighboring atoms. The W phases within the pristine lattice have a similar distance as the minimum in Fig. 1b resulting in the lower phase observed. Therefore, the phase of each atom in a lattice is visually reduced compared to an isolated atom. Such effects are not accounted for using simple integration methods of quantification. Note that this is in contrast to Z-contrast ADF imaging, where no negative halos exist, only positive definite probe tails. This is important when, for instance, the sample tilts and the projected interatomic distances are changed, altering the phase of the atomic sites without meaningful change in the potential itself.

To account for this non-linear contrast formation, we introduce a new method which reliably and accurately extracts the phase corresponding to the actual potential for the atoms in arbitrary networks and orientations, and demonstrate it with defective WS_2 as shown Fig. 1c. The method optimizes a point-potential which is convolved

with a kernel. Here we focus on the contrast transfer function (CTF) for SSB, although other kernels can be used for other imaging modes, as we demonstrate for ePIE and iCoM. The SSB kernel has the same shape as an isolated SSB reconstructed atom such as in Fig. 1a and can be interpreted as the point spread function (PSF). The point-potential represents the atomic positions as well as their phase. We compare this new “SSB-CTF based” kernel with a kernel generated by the “ADF-CTF” which is very similar to a Gaussian kernel. The analysis with the ADF-CTF based kernel is very similar to simple Gaussian-fitting [21] or Voronoi-integration [17] in the absence of aberrations [22]. The new method reliably and accurately extracts the deconvolved phases and, importantly, is robust to environmental changes such as local atomic configuration and sample tilt. Our new method in principle makes quantitative analysis of phase images with arbitrary contrast transfer functions possible.

2. Methods

2.1. Computational method

The method works by iteratively updating the atomic positions and their point potential representations such that images simulated using the convolution of the point potentials by the PSF match the input images as closely as possible. Fig. 2 illustrates the process using defective WS_2 as an example, and the complete method is summarized in a flow chart in Fig. 3. The WS_2 model in Fig. 2a results in the point-potential image shown in b.

In general, the 2D point potential takes the form

$$V(\mathbf{r}) = \sum_{\mathbf{r}_Z} \Phi_{\mathbf{r}_Z} \cdot \delta_{\mathbf{r},\mathbf{r}_Z} \quad (1)$$

where \mathbf{r}_Z are the exact positions of the atoms in the model M and δ is the Kronecker delta function, being one if $\mathbf{r} = \mathbf{r}_Z$ and zero otherwise. We chose Φ as the variable for non-zero pixel values as they represent the phase cross-section of the atoms. In practise, the potential is calculated by iterating through all atoms and adding the corresponding phase value at the corresponding pixel position. For spatial precision, sub-pixel precision is enabled by weighting four neighboring pixels in the potential map, as the potential maps have the sample pixel dimensions as the input images, which can be coarser than the positions of the atoms. In practise, the initial model is often relatively easy to match to the experimental data manually via scaling and translations.

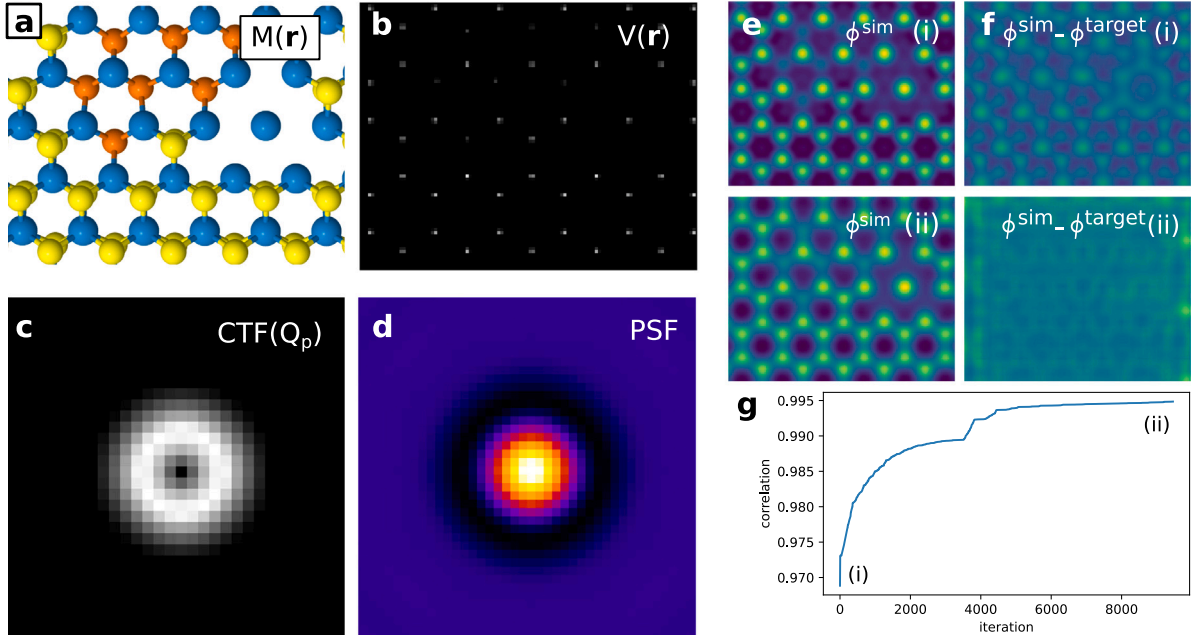


Fig. 2. Illustration of the steps in the procedure for phase quantification. (a) The initial atomic model containing the correct elements and the approximate positions is converted to (b) a point-potential based on the model. (c) The calculated CTF of SSB ptychography is converted to the PSF by FFT as illustrated in (d). (e) Initial (i) and optimized (ii) convolutional simulations. As can be seen in the difference images in (f), showing the convolutional simulations minus the target image, the difference has been greatly reduced from the initial result (i) in the optimized image (ii). One can also see how the optimization increases the correlation function as a function of iteration in (g).

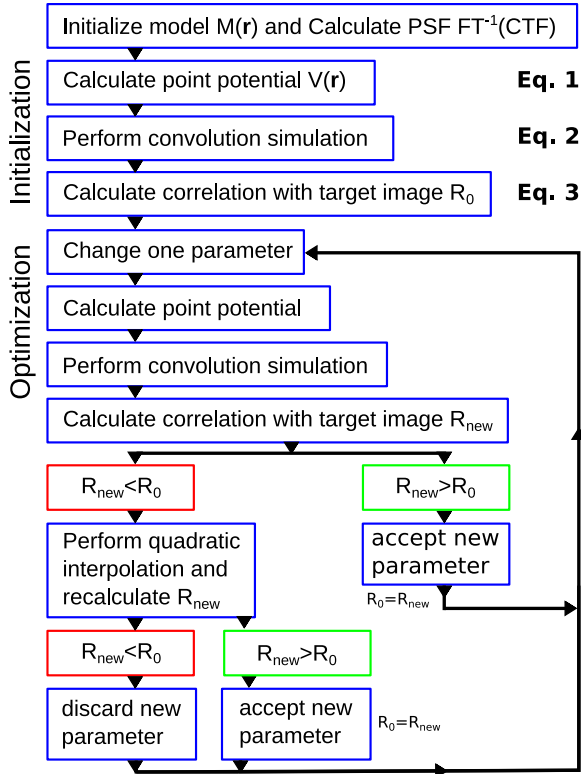


Fig. 3. Flow chart of the phase extraction algorithm.

Once a point potential map is produced, a phase image, ϕ , is simulated simply by convolving the potential with the chosen PSF [23], the inverse Fourier transform of the CTF,

$$\phi^{sim} = V(\mathbf{r}) * FT^{-1}(CTF(Q_p)). \quad (2)$$

The error is then calculated between the convolutionally simulated image, ϕ^{sim} , and the input phase image, ϕ^{target} , and the positions of the atoms in the model and their point potential values are then iteratively updated such that the difference between the image simulated from the point potential map and the input image is minimized. In addition the algorithm optimizes the PSF width, which can be altered by either the convergence angle or the field of view via the probe position step size. The optimization process is described in detail below. Using convolutional simulations is advantageous for the speed of the computations, but by optimizing a single value of the potential for each atomic site in this way, the point is also to provide the best possible quantification of “the phase” of an atom or atomic column, including the effect of screening by electrons which are distributed further away from the nucleus [13].

2.1.1. CTFs

The SSB CTF is related to the geometric size of the double disk overlaps for each spatial frequency Q_p for a given convergence angle α [19] as

$$CTF(Q_p) = \frac{4}{\pi} \cdot \left[\cos^{-1}\left(\frac{Q_p}{2}\right) - \frac{Q_p}{2} \cdot \sqrt{1 - \left(\frac{Q_p}{2}\right)^2} - \cos^{-1}(Q_p) + Q_p \cdot \sqrt{1 - (Q_p)^2} \right]$$

for $0 \leq Q_p \leq \alpha$ and

$$CTF(Q_p) = \frac{4}{\pi} \cdot \left[\cos^{-1}\left(\frac{Q_p}{2}\right) - \frac{Q_p}{2} \cdot \sqrt{1 - \left(\frac{Q_p}{2}\right)^2} \right]$$

for $\alpha < Q_p \leq 2\alpha$ and 0 otherwise. The 2D CTF of SSB is shown in Fig. 2c and the real space transformation of this, the PSF, in panel d, which in this paper, we refer to as the SSB CTF based kernel.

Note that the PSF (Fig. 2d), the inverse Fourier transform of the CTF, is a result of coherent interference and contains negative values. In contrast, the ADF-based PSF is obtained via Zernike polynomials and the result of the inverse Fourier transform is squared as a result of the

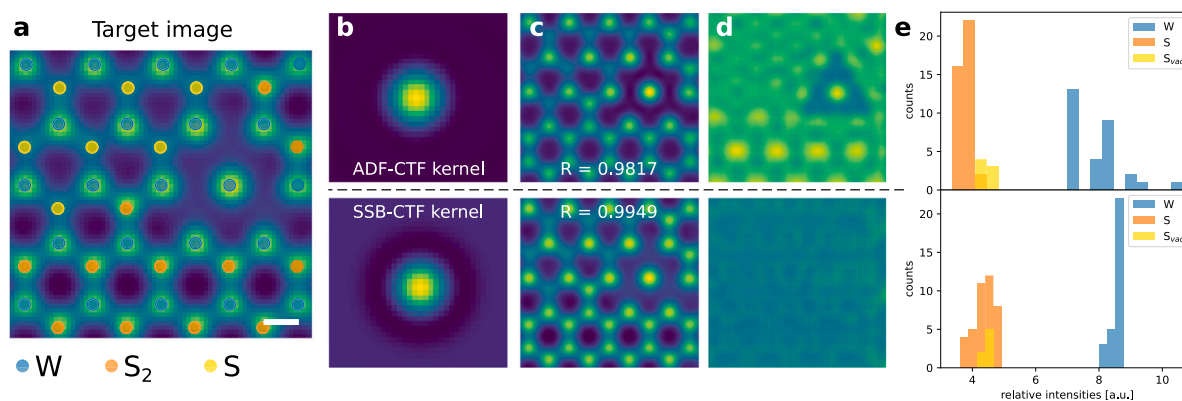


Fig. 4. Comparison between phase extraction using a Gaussian kernel based on an ADF-CTF and a SSB-CTF based kernel. (a) Target image which is used as benchmark for the methods. (b) ADF-CTF based and SSB-CTF based kernel. (c) Optimized convolution simulation using the ADF-based kernel and SSB-based kernel in top and bottom, respectively. (d) Difference image between (a) and (c). (e) Extracted phases using both kernels.

incoherent image formation process. We further note that an alternative to an analytical calculation of the CTF is to extract the CTF numerically from simulations of an isolated atom via the same algorithm as used for the target image. This is indeed possible as the exact profile is negligibly dependent on the element [18]. The code can be found on Gitlab [24].

2.1.2. Optimization

To quantify the merit of a particular configuration we use the correlation between the input target image and the convolutional simulation

$$R = \sum_{i=1}^N \frac{(\mu^{\text{sim}} - \phi_i^{\text{sim}})(\mu^{\text{target}} - \phi_i^{\text{target}})}{\sigma^{\text{sim}}\sigma^{\text{target}}(N-1)}, \quad (3)$$

with μ being the mean value and σ being the standard deviation. The sum iterates through all pixel values ϕ of the convolutional simulation and the input target image. This is shown in Fig. 2e for the initial and optimized simulation in top and bottom, respectively. The correlation function is maximized by adjusting the parameters for the atomic positions, width of the kernel and the strength of the potential. The difference images for both cases are shown in (f). The correlation in the course of the optimization is shown in (g). This function is maximized based on quadratic interpolation where the gradients in each direction are calculated by the finite difference method and the minimum of a quadratic fit is estimated to be the next iteration value. The source size can also be optimized, and the atomic positions collectively changed by applying translations, scalings, rotations and importantly sample tilts. This is crucial for experimental conditions, where a sufficient alignment between the simulation of the model and the experimental image is the task of the optimization.

3. Results and discussion

To compare a conventional integration of the atomic sites with the new method, we performed the optimization analysis with an ADF-CTF based kernel and an SSB-CTF based kernel. The target input image is the quantitative SSB simulation of defective WS_2 shown in Fig. 4a, where the positions are labeled with blue (W), yellow (S vacancies) and orange (S_2). The convergence angle is set to 20 mrad and the acceleration voltage to 60 kV. The target input simulation is based on an independent atomic model potential, in which electron redistribution is not taken into account. Therefore, the same elements have the same phase in the phase image which is an ideal test for the different methods. The ADF-CTF based kernel is very similar to a Gaussian kernel and the analysis with it is very similar to simple Gaussian-fitting [21] or Voronoi-integration [17] in the absence of aberrations [22]. However, we will show that this approach is problematic for quantifying SSB

images as the phase of the atoms also depends on the local environment, as discussed in the introduction. The second kernel is obtained via the SSB-CTF, as described in the Methods section. Accounting for the negative halo in the kernel, which is also visible in the single atom SSB reconstruction shown in Fig. 1a, is crucial for an accurate analysis. Both kernels are shown in Fig. 4b.

When optimizing the simulations using the atomic positions and point-potential values as parameters, both methods result in similar looking simulated images (cf. Fig. 4c). However, the images showing the difference between the optimized convolutional simulations and the input target image, reveal significant residual features in the case of the ADF-CTF based image (cf. panel d). This is because the contrast cannot be perfectly matched in this case. The difference image using the SSB-CTF kernel is almost perfectly flat as a result of an excellent match between the simulation and the target image. This is reflected in the higher correlation coefficient in the SSB-CTF kernel based optimization.

Importantly, significant errors appear in the resulting extracted phases of the optimized point-potentials. When using the ADF-based kernel simulation, the histogram of phases (Fig. 4e) shows a more scattered W phase value distribution as the stronger phase of W close to weaker potentials (e.g. vacancies) has to be matched by increasing the point-potential, when in fact the potential of this site is identical to the other W sites. The highest peak corresponds to the isolated W, surrounded by double vacancies in the structure, due to the contrast reduction for the W atoms within the pristine lattice. Also, the S atoms in the S_2 sites (orange) are slightly lower than the single S vacancies (yellow) due to the same reason (see Fig. 4e top). This makes the phase extraction unreliable as the contrast transfer functions are not properly taken into account. Using the SSB-CTF kernel gives, however, a much sharper histogram as the local environment is taken into account. Again, keep in mind that this is an independent atom model so the variation should be essentially nil across sites with the same elements and number of atoms. Correctly accounting for the CTF makes the interpretation of the phases due to actual changes in the material, such as bonding, much easier and much more reliable. Note that the width of S (orange) in the S_2 site is unavoidably larger because they are pairwise overlapping in the projection. However, their mean value is matching the S vacancy values (yellow) as expected for the target image. Also the W atoms show much less variation despite the non-linear contrast formation. This is important for detecting small differences between atomic sites, which occurs for example when detecting charge transfer.

The strong dependency of the SSB contrast on the local environment also makes quantification difficult when small sample tilts are present as these lead to small projected positional shifts of the atoms. Small tilts are difficult to measure in STEM experiments and residual sample tilts are practically unavoidable. The contrast dependency of the sample tilt is demonstrated in Fig. 5a and b, which show IAM-based SSB

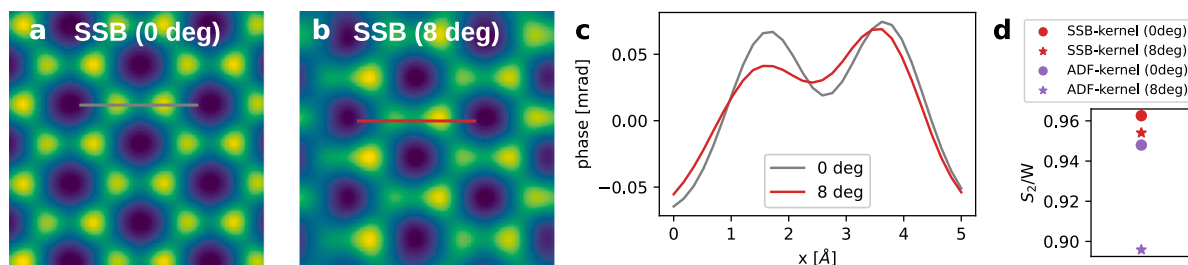


Fig. 5. Specimen tilt sensitivity of ptychographic reconstructions. SSB images of (a) untilted and (b) 8 degree tilted WS_2 . (c) Line profiles of (a) and (b). (d) Extracted phases using a Gaussian kernel (purple) and a SSB-CTF based kernel (red).

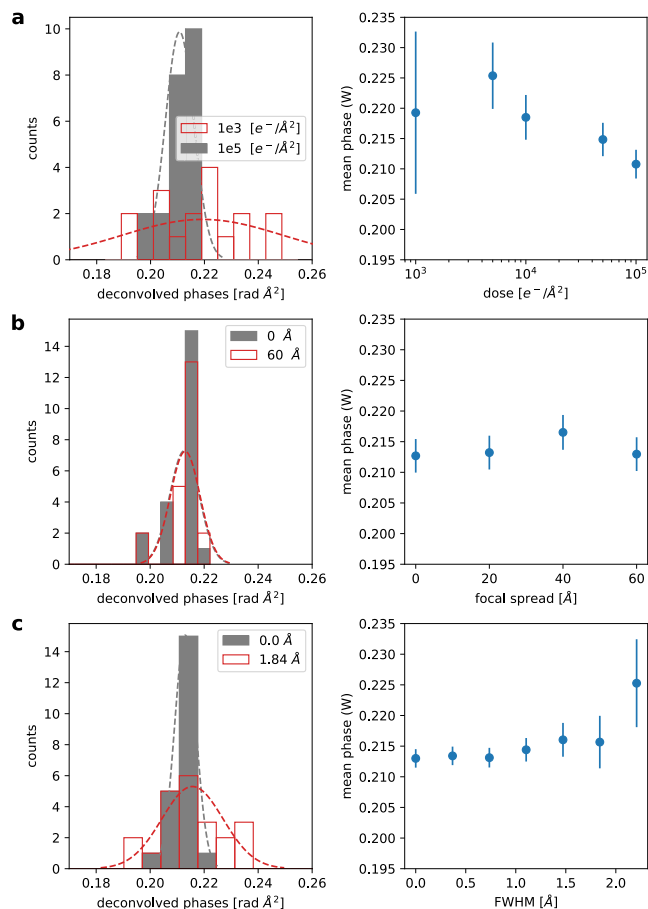


Fig. 6. Precision of the optimization method under different conditions. Analysis of SSB phase extraction with different electron doses (a), with and without temporal incoherence (b) and with and without the effect of finite source sizes (c). Each panel shows the extracted phases of two conditions (left) and the mean values as well as the error bars (right).

simulations of untilted and 8 degrees tilted WS_2 respectively. The contrast change is shown by the line profile (panel c), where the S_2 sites show a significantly reduced phase when tilted. To demonstrate the robustness of the optimization method to sample tilt, we performed the quantification analysis on both the untilted and tilted images using both the SSB and ADF based kernels. For the untilted pristine case, both kernels give similar S_2 to W ratios. However, analyzing the tilted image gives a remarkable deviation when using the ADF-kernel (5.50%) while the difference using the SSB-CTF based kernel is much lower (0.89%). Ideally mistilt should be avoided experimentally, but this method can greatly reduce the influence of mistilt, making it potentially insignificant compared to other influences such as limited electron dose. This shows the robustness of the new phase extraction method

to sample tilt. To make this happen, the sample tilt is included in the optimization which gives the correct value based on the distortion of the lattice. Importantly, this requires that scan distortion is minimized, which is now possible in 4D STEM based on truly fast cameras that enable microsecond level dwell times, such as event-based cameras [7].

Next we investigated the robustness of the phase extraction to other typical experimental influences. We measured the W phase as a function of electron dose, partial coherence and source size individually. The resulting phases are shown in Fig. 6. For common operating conditions, by far the largest deleterious influence on the precision is when a limited amount of signal per diffraction pattern is available, as a result of a limited electron dose imparted to the specimen. This is shown in Fig. 6a. However the error bar of the mean value not only depends on the dose but also on the number of atomic sites analyzed. To evaluate if the error bar is small enough in the context of analyzing phase differences, for example due to the subtle changes occurring with charge transfer due to bonding, the difference between the involved phases has to be considered. We analyzed the charge transfer of WS_2 where the phase difference was indeed large enough to detect the difference caused by charge transfer at moderate doses [25]. The partial coherence is simulated via a defocus spread ranging from 0–6 nm. Typical values are around 3 nm for a cold FEG, greater for less coherent sources. The phase change is small because of the robustness of ptychography to partial coherence [3]. Lastly, the source size is simulated by using a Gaussian blur up to a FWHM 2.3 Å. The phase change is insignificant for typical source sizes [26]. We therefore conclude that dose, and by extension the sample stability, are the most crucial parameters determining if phase variations due to physical variation in the sample potential are detectable.

Phase retrieval methods can encounter the issue of phase wraps with strong potentials. This means when increasing the strength of the potential, the resulting atomic phase wraps to a negative value in the center of the atomic columns as has been observed in both simulations and experiments. At this point, the atoms deviate from their natural rotational symmetric shape and the presented method is not reliable. However, it has been shown that these effects can be corrected by adjusting the probe defocus post collection [9]. However, as the ptychographic contrast mechanism becomes more complex when the sample gets thicker we consider the present method to be reliable for thin materials such as 2D materials. The application of this method to thicker materials is beyond the scope of this paper and will be investigated in future work.

Our method is in principle also applicable to imaging methods with other CTFs. The choice of CTF results in different kernel shapes representing the shape of an individual atom in the final phase image [18]. This makes the method very flexible to use, including for noise-normalized contrast transfer functions. Here, we analyze the phase retrieved by iterative ptychography with the extended ptychographic iterative engine (ePIE) as an example. We simulated the same region as the other examples via ePIE which has a different CTF and therefore a different PSF than SSB, as shown in Fig. 7a. Since the exact CTF depends on the algorithm, we provided the kernel by simulating a single atom with the same algorithm. We used an 0.5 Å probe position

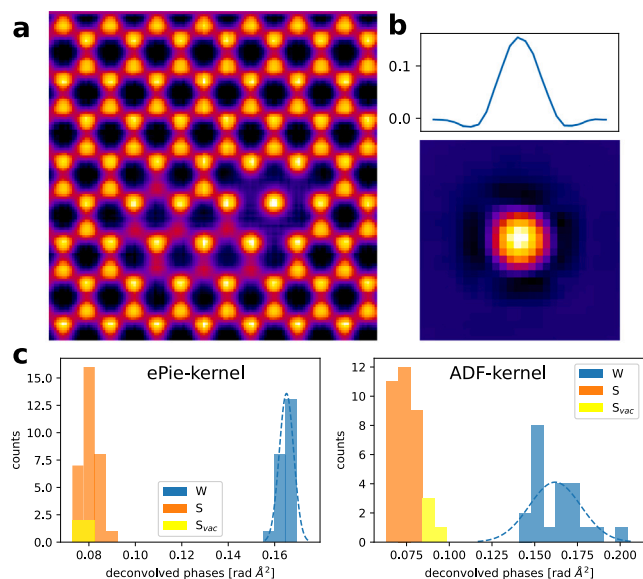


Fig. 7. Kernel method quantification of iterative ptychography using ePIE. (a) ePIE reconstruction of defective WS₂. (b) Line profile and 2D image of PSF of ePIE. (c) Extracted phases of (a) using the ePIE kernel (left) and a Gaussian kernel (right). ePIE also exhibits a PSF with a negative halo which enhances the phase of an isolated atom compared to atoms with neighbors. This can be correctly accounted for using the ePIE PSF with our method in quantification.

step size, a 1 nm defocus and the same 20 mrad convergence angle used earlier. Interestingly, it also shows a negative halo, similar to the SSB, but somewhat less pronounced (Fig. 7b). Therefore, the W within the defective network is also brighter than the W atoms within the pristine lattice with ePIE. As with SSB data, the kernel method again correctly accounts for this when using the ePIE-based kernel. The extracted phases show, similar to the SSB, sharp peaks in the case of the optimization using the ePIE-PSF. Using the Gaussian-shaped PSF from the ADF kernel on the ePIE data, results in a much broader width of the distribution of W phases, as expected (cf. Fig. 7c).

We also analyzed integrated center-of-mass (iCoM) imaging as a further 4D STEM imaging method. iCoM is becoming increasingly popular with the development of fast cameras since it is a more accurate method compared to the now popular integrated differential phase contrast (iDPC) imaging modality. However, both images can be analyzed similarly as outlined below. The only difference is the non-rotationally symmetric CTF of iDPC as a result of the segmentation of the detector, which would need to be accounted for correctly for an accurate analysis of iDPC images, and therefore the exact detector geometry with respect to the diffraction patterns would have to be known. iCoM is very simple and fast and therefore a reliable tool for live iCoM imaging [27]. However, it has been observed to be less dose efficient than ptychographic methods [9,28]. It also cannot correct residual aberrations and has no super-resolution ability. Since the CTF of iCoM is starting at 1 [29], there are no artifacts associated with the negative part of the PSF when used with the raw data. However, high pass filters are commonly applied to iCoM and iDPC data, and real-time iCoM (riCoM) contains an intrinsic filtering depending on the riCoM kernel used. In all these cases the PSF for iCoM, and by extension iDPC, obtains a negative contribution similar to the discussions above. This is demonstrated in Fig. 8 where raw and high pass filtered iCoM images of the same defective WS₂ region are shown. Such filtering is very commonly used to sharpen iCoM or iDPC images generally or ameliorate the effect of contamination, as well as edge artifacts. Importantly, the isolated W atom is also brighter here in the case of the filtered image. This is, once again, a result of the PSF which shows a negative tail in case of the filtered image. Therefore, conventional quantification

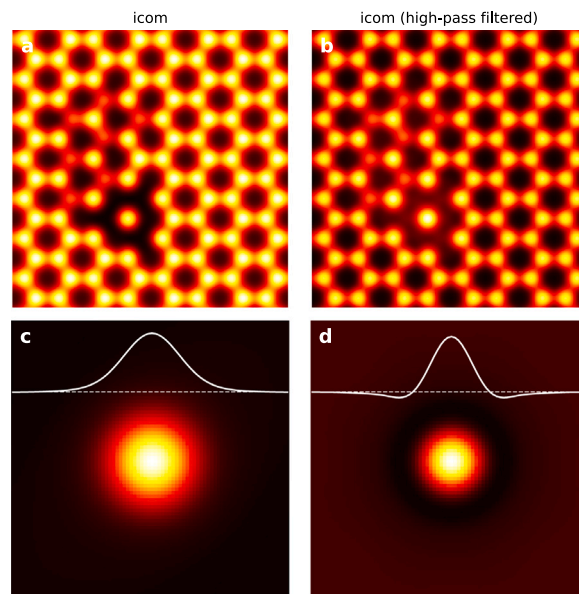


Fig. 8. Filter effect on phase quantification of iCoM (a) Raw iCoM reconstruction of defective WS₂. (b) Same as (a) but with a high-pass filter. (c,d) PSF of (a) and (b), respectively. Notice that the filter causes a negative halo in the PSF of the iCoM which again enhances the brightness of isolated atoms compared to those with close neighbors. This can be accounted for with our kernel quantification method.

of high-pass filtered iCoM and iDPC images will encounter similar problems as in the SSB image analysis in that the extracted phases highly depend on the environmental conditions. Omitting the high pass filter however also often leads to unreliable quantification as the low-frequency contribution harms the image analysis [30]. Therefore, a reliable quantification of iCoM and iDPC phases is only possible via a method such as the optimization method we have presented in which the exact filter conditions are reproduced in the PSF. This is usually facile since the filter parameters are usually very accurately known.

4. Conclusion

We have introduced a new method to reliably analyze ptychographic phase images quantitatively. The method takes into account the specific contrast transfer function and is therefore robust to local environments such as atomic configuration and sample tilts. This is very important when tiny changes of the phase images are analyzed, such as with charge transfer due to bonding. We believe this method opens a path towards a reliable quantification of phase images as it has been achieved for ADF images.

Declaration of competing interest

The authors declare that they have no known competing financial interests or personal relationships that could have appeared to influence the work reported in this paper.

Data availability

We share our code in a public repository which we mention in the manuscript.

Acknowledgments

We acknowledge funding from the European Research Council (ERC) under the European Union's Horizon 2020 Research and Innovation Programme via Grant Agreement No. 802123-HDEM and FWO Project G013122N "Advancing 4D STEM for atomic scale structure property correlation in 2D materials" (C.H.).

References

- [1] F. Hüe, J.M. Rodenburg, A.M. Maiden, F. Sweeney, P.A. Midgley, Wave-front phase retrieval in transmission electron microscopy via ptychography, *Phys. Rev. B* 82 (2010) 121415, <http://dx.doi.org/10.1103/PhysRevB.82.121415>, URL <https://link.aps.org/doi/10.1103/PhysRevB.82.121415>.
- [2] P.D. Nellist, B.C. McCallum, J.M. Rodenburg, Resolution beyond the “information limit” in transmission electron microscopy, *Nature* 374 (6523) (1995) 630–632, <http://dx.doi.org/10.1038/374630a0>.
- [3] T.J. Pennycook, G.T. Martinez, P.D. Nellist, J.C. Meyer, High dose efficiency atomic resolution imaging via electron ptychography, *Ultramicroscopy* 196 (2019) 131–135, <http://dx.doi.org/10.1016/j.ultramic.2018.10.005>, URL <https://www.sciencedirect.com/science/article/pii/S0304399118302316>.
- [4] Z. Chen, M. Kronenberg, Y. Jiang, Y. Han, M.-H. Chiu, L. Li, D. Muller, Mixed-state electron ptychography enables sub-angstrom resolution imaging with picometer precision at low dose, *Nature Communications* 11 (2020) <http://dx.doi.org/10.1038/s41467-020-16688-6>.
- [5] J. Song, C. Allen, S. Gao, C. Huang, H. Sawada, X. Pan, J. Warner, P. Wang, A. Kirkland, Atomic resolution defocused electron ptychography at low dose with a fast, direct electron detector, *Sci. Rep.* 9 (2019) <http://dx.doi.org/10.1038/s41598-019-40413-z>.
- [6] L. Zhou, J. Song, J. Kim, X. Pei, C. Huang, M. Boyce, L. Mendonça, D. Clare, A. Siebert, C. Allen, E. Liberti, D. Stuart, X. Pan, P. Nellist, P. Zhang, A. Kirkland, P. Wang, Low-dose phase retrieval of biological specimens using cryo-electron ptychography, *Nature Commun.* 11 (2020) <http://dx.doi.org/10.1038/s41467-020-16391-6>.
- [7] D. Jannis, C. Hofer, C. Gao, X. Xie, A. Béché, T. Pennycook, J. Verbeeck, Event driven 4D STEM acquisition with a Timepix3 detector: Microsecond dwell time and faster scans for high precision and low dose applications, *Ultramicroscopy* 233 (2022) 113423, <http://dx.doi.org/10.1016/j.ultramic.2021.113423>, URL <https://www.sciencedirect.com/science/article/pii/S0304399121001996>.
- [8] H. Yang, R. Rutte, L. Jones, M. Simson, R. Sagawa, H. Ryll, M. Huth, T. Pennycook, M. Green, H. Soltau, Y. Kondo, B. Davis, P. Nellist, Simultaneous atomic-resolution electron ptychography and Z-contrast imaging of light and heavy elements in complex nanostructures, *Nature Commun.* 7 (2016) 12532, <http://dx.doi.org/10.1038/ncomms12532>.
- [9] C. Gao, C. Hofer, D. Jannis, A. Béché, J. Verbeeck, T.J. Pennycook, Overcoming contrast reversals in focused probe ptychography of thick materials: An optimal pipeline for efficiently determining local atomic structure in materials science, *Appl. Phys. Lett.* 121 (8) (2022) 081906, <http://dx.doi.org/10.1063/5.0101895>, [arXiv:https://doi.org/10.1063/5.0101895](https://doi.org/10.1063/5.0101895).
- [10] J. Madsen, T.J. Pennycook, T. Susi, Ab initio description of bonding for transmission electron microscopy, *Ultramicroscopy* 231 (2021) 113253, <http://dx.doi.org/10.1016/j.ultramic.2021.113253>, URL <https://www.sciencedirect.com/science/article/pii/S0304399121000449>, 80th Birthdays of Colin Humphreys and Knut Urban, 75th Birthdays of Wolfgang Baumeister and John Spence - PICO 2021 – Sixth Conference on Frontiers of Aberration Corrected Electron Microscopy.
- [11] K. Müller-Caspary, F.F. Krause, T. Grieb, S. Löffler, M. Schowalter, A. Béché, V. Galioit, D. Marquardt, J. Zweck, P. Schattschneider, J. Verbeeck, A. Rosenauer, Measurement of atomic electric fields and charge densities from average momentum transfers using scanning transmission electron microscopy, *Ultramicroscopy* 178 (2017) 62–80, <http://dx.doi.org/10.1016/j.ultramic.2016.05.004>, URL <https://www.sciencedirect.com/science/article/pii/S0304399116300596>, FEMMS 2015.
- [12] W. Gao, C. Addiego, H. Wang, X. Yan, Y. Hou, D. Ji, C. Heikes, Y. Zhang, L. Li, H. Huyan, T. Blum, T. Aoki, Y. Nie, D.G. Schlom, R. Wu, X. Pan, Real-space charge-density imaging with sub-ångström resolution by four-dimensional electron microscopy, *Nature* 575 (7783) (2019) 480–484, <http://dx.doi.org/10.1038/s41586-019-1649-6>.
- [13] G.T. Martinez, T.C. Naginey, L. Jones, C.M. O’Leary, T.J. Pennycook, R.J. Nicholls, J.R. Yates, P.D. Nellist, Direct imaging of charge redistribution due to bonding at atomic resolution via electron ptychography, 2019, <http://dx.doi.org/10.48550/ARXIV.1907.12974>, URL <https://arxiv.org/abs/1907.12974>.
- [14] J. Meyer, S. Kurasch, H. Park, V. Skákalová, D. Künzel, A. Gross, A. Chuvpilo, G. Algara-Siller, S. Roth, T. Iwasaki, U. Starke, J. Smet, U. Kaiser, Experimental analysis of charge redistribution due to chemical bonding by high-resolution transmission electron microscopy, *Nat. Mater.* 10 (2011) 209–215, <http://dx.doi.org/10.1038/nmat2941>.
- [15] G. Martinez, K. van den Bos, M. Alania, P. Nellist, S. Van Aert, Thickness dependence of scattering cross-sections in quantitative scanning transmission electron microscopy, *Ultramicroscopy* 187 (2018) 84–92, <http://dx.doi.org/10.1016/j.ultramic.2018.01.005>, URL <https://www.sciencedirect.com/science/article/pii/S0304399117303194>.
- [16] O. Krivanek, M. Chisholm, V. Nicolosi, T. Pennycook, G. Corbin, N. Dellby, M. Murfitt, C. Own, Z. Szilagyí, M. Oxley, S. Pantelides, S. Pennycook, Atom-by-atom structural and chemical analysis by annular dark-field electron microscopy, *Nature* 464 (2010) 571–574, <http://dx.doi.org/10.1038/nature08879>.
- [17] H. E. K. MacArthur, T. Pennycook, E. Okunishi, A. D’Alfonso, N. Lugg, L. Allen, P. Nellist, Probe integrated scattering cross sections in the analysis of atomic resolution HAADF STEM images, *Ultramicroscopy* 133 (2013) 109–119, <http://dx.doi.org/10.1016/j.ultramic.2013.07.002>, URL <https://www.sciencedirect.com/science/article/pii/S0304399113001770>.
- [18] C.M. O’Leary, G.T. Martinez, E. Liberti, M.J. Humphry, A.I. Kirkland, P.D. Nellist, Contrast transfer and noise considerations in focused-probe electron ptychography, *Ultramicroscopy* 221 (2021) 113189, <http://dx.doi.org/10.1016/j.ultramic.2020.113189>, URL <https://www.sciencedirect.com/science/article/pii/S0304399120303314>.
- [19] H. Yang, T.J. Pennycook, P.D. Nellist, Efficient phase contrast imaging in STEM using a pixelated detector. part II: Optimisation of imaging conditions, *Ultramicroscopy* 151 (2015) 232–239, <http://dx.doi.org/10.1016/j.ultramic.2014.10.013>, URL <https://www.sciencedirect.com/science/article/pii/S0304399114002058>, Special Issue: 80th Birthday of Harald Rose; PICO 2015 – Third Conference on Frontiers of Aberration Corrected Electron Microscopy.
- [20] T.J. Pennycook, A.R. Lupini, H. Yang, M.F. Murfitt, L. Jones, P.D. Nellist, Efficient phase contrast imaging in STEM using a pixelated detector. part I: Experimental demonstration at atomic resolution, *Ultramicroscopy* 151 (2015) 160–167, <http://dx.doi.org/10.1016/j.ultramic.2014.09.013>, URL <https://www.sciencedirect.com/science/article/pii/S0304399114001934>, Special Issue: 80th Birthday of Harald Rose; PICO 2015 – Third Conference on Frontiers of Aberration Corrected Electron Microscopy.
- [21] S. Van Aert, J. Verbeeck, R. Erni, S. Bals, M. Luysberg, D.V. Dyck, G.V. Tendeloo, Quantitative atomic resolution mapping using high-angle annular dark field scanning transmission electron microscopy, *Ultramicroscopy* 109 (10) (2009) 1236–1244, <http://dx.doi.org/10.1016/j.ultramic.2009.05.010>, URL <https://www.sciencedirect.com/science/article/pii/S0304399109001259>.
- [22] C. Hofer, V. Skákalová, J. Haas, X. Wang, K. Braun, R.S. Pennington, J.C. Meyer, Atom-by-atom chemical identification from scanning transmission electron microscopy images in presence of noise and residual aberrations, *Ultramicroscopy* 227 (2021) 113292, <http://dx.doi.org/10.1016/j.ultramic.2021.113292>, URL <https://www.sciencedirect.com/science/article/pii/S0304399121000802>.
- [23] E.J. Kirkland, *Advanced Computing in Electron Microscopy*, second ed., Springer US, New York, 2010, <http://dx.doi.org/10.1007/978-1-4419-6533-2>.
- [24] C. Hofer, Stem optimization, GitLab repository (2022) https://gitlab.com/christopher_hofer/stem_optimization.
- [25] C. Hofer, J. Madsen, T. Susi, T.J. Pennycook, Detecting charge transfer in defective 2D WS₂ with electron ptychography, 2023, [arXiv:2301.04469](https://arxiv.org/abs/2301.04469).
- [26] J. Verbeeck, A. Béché, W. Van den Broek, A holographic method to measure the source size broadening in STEM, *Ultramicroscopy* 120 (2012) 35–40, <http://dx.doi.org/10.1016/j.ultramic.2012.05.007>, URL <https://www.sciencedirect.com/science/article/pii/S030439911200109X>.
- [27] C.-P. Yu, T. Friedrich, D. Jannis, S. Van Aert, J. Verbeeck, Real-Time Integration Center of Mass (riCOM) Reconstruction for 4D STEM, *Microsc. Microanal.* 28 (5) (2022) 1526–1537, <http://dx.doi.org/10.1017/S1431927622000617>, [arXiv:https://academic.oup.com/mam/article-pdf/28/5/1526/48814282/mam1526.pdf](https://academic.oup.com/mam/article-pdf/28/5/1526/48814282/mam1526.pdf).
- [28] C.M. O’Leary, C.S. Allen, C. Huang, J.S. Kim, E. Liberti, P.D. Nellist, A.I. Kirkland, Phase reconstruction using fast binary 4D STEM data, *Appl. Phys. Lett.* 116 (12) (2020) 124101, <http://dx.doi.org/10.1063/1.5143213>, [arXiv:https://pubs.aip.org/aip/apl/article-pdf/doi/10.1063/1.5143213/14532254/124101_1_online.pdf](https://pubs.aip.org/aip/apl/article-pdf/doi/10.1063/1.5143213/14532254/124101_1_online.pdf).
- [29] I. Lazić, E.G. Bosch, S. Lazar, Phase contrast STEM for thin samples: Integrated differential phase contrast, *Ultramicroscopy* 160 (2016) 265–280, <http://dx.doi.org/10.1016/j.ultramic.2015.10.011>, URL <https://www.sciencedirect.com/science/article/pii/S0304399115300449>.
- [30] E. Yücelen, I. Lazić, E.G.T. Bosch, Phase contrast scanning transmission electron microscopy imaging of light and heavy atoms at the limit of contrast and resolution, *Sci. Rep.* 8 (1) (2018) 2676, <http://dx.doi.org/10.1038/s41598-018-20377-2>, <https://europemc.org/articles/PMC5805791>.